Supplementary Information: Dynamic Cross-Linking of an Alginate-Acrylamide Tough Hydrogel System: Time-Resolved In Situ Mapping of Gel Self-Assembly

Akanksha Pragya[a]^, Suhas Mutalik[a]^, Muhammad Waseem Younas[a]^, Siu-Kwong Pang[a]^, Pui-Kin So[b], Faming Wang[b], Zijian Zheng[a], and Nuruzzaman Noor[a].*

^These authors contributed equally to the manuscript.

[a] Pragya, A.; Mutalik, S.; Younas, M.W.; Pang, S-K.; Zheng, Z.; & N. Noor*****. The Hong Kong Polytechnic University, Institute of Textiles and Clothing, Materials Synthesis and Processing Lab, Hung Hom, Kowloon, Hong Kong SAR, China. E-mail: nmnoor@polyu.edu.hk.

[b] So, P-K. The Hong Kong Polytechnic University, University Research Facility in Life Sciences, Hung Hom, Kowloon, Hong Kong SAR, China.

[c] Wang, F. Central South University, School of Architecture and Art, Changsha, China.

1. Methodology

a. Chemicals

Tough hydrogels were synthesised as outlined in the manuscript methodology. Molar equivalent of cationic cross-linker were substituted for the $CaSO_4$. Calcium lignosulfate (CaLs; Aladin), sodium sulphate anhydrous (Na_2SO_4; Unichem), magnesium sulphate anhydrous ($MgSO_4$; Guangzhou Chemical Reagent Factory), and; calcium chloride anhydrous ($CaCl_2$; Sigma-Aldrich; min. 93%).

b. Characterisation

For Matrix-assisted laser desorption/ionization–Time-of-Flight Mass Spectrometry (MALDI-TOF MS) analysis, samples were prepared by dissolving 10mg.ml^{-1} of sodium alginate solution in 70%ACN/30%H_2O containing 0.1% trifluoroacetic acid. The sodium alginate solution was then mixed with equal volume of 10 mg.ml^{-1} 2,5-dihydroxybenzoic acid matrix in the same solvent system. A 1 uL aliquot of the sample/matrix solution was loaded onto a stainless steel MALDI-MS target plate for analysis. MALDI-TOF MS data was obtained on a *Bruker UltrafleXtreme MALDI-TOF/TOF-MS* equipped with a 355 nm Nd/YAG laser (3 ns laser pulse width). The MS was operated in positive reflectron mode and the reflector voltage and laser repetition rate were set at 21.1 kV and 2000 Hz, respectively. MALDI-MS spectra were obtained with accumulation of 2000 laser shots. Time-lapsed fluorescence imaging was carried out on a Ti2-E live cell imaging system with a 25 mm FOV, and CFI Plan Apo 60x/1.40 Oil as an objective, with a R6G tracer dye.[1–3] The wavelength channel used for excitation was 460-500 nm with a FITC filter set. Image sequences were converted from colour (24-bit red, green, and blue (RGB)).bmp files to 8-bit grayscale.bmp files using *ImageJ* software. Images were acquired at 1600×1200 pixels with a 0.184-µm.pixel^{-1} spatial dimension. For manual tracking, the *MtrackJ* and the *Chemotaxis* tool plugins were used; images were extracted from auto-focused z-stacks, then denoised, deconvoluted and registered.[4,5] Time-lapse micro-scale imaging was carried out on *Leica* optical microscopy (M165C; ASTM D3576), and macro-scale imaging done on an iPhone Xs at 1080p resolution. Multimedia files are given as

Supporting Information (see SI V1-3). DLS analyses were carried out on a *Brookhaven Instruments Corporation ZetaPlus Potential Analyzer*; TGA-DSC tests on a *Mettler-Toledo Star e TGA Thermogravimetric Analyzer*, under N_2 (20 $mL.min^{-1}$) in dynamic mode, at a 10°C.min^{-1} ramp rate, over the 50-590°C range; Wide angle X-ray diffraction (WAXD) was employed to identify the presence of any crystalline matter in the composite structures, and collected on a *Rigaku SmartLab* X-ray diffractometer with Cu Kα radiation (λ = 1.542 Å), operating at 45 kV and 200 mA, over the 20–80° 2θ angle range at a step size of 0.01; UV-visible spectroscopy (*UH5300 Hitachi*) recorded at 1 nm step, across 200-800 nm, at 400 nm.min^{-1} against a DI-H_2O reference standard; Raman spectroscopy (*BaySpec Nomadic*) with a 532 nm laser excitation source (100% intensity), over 200–3200 cm^{-1}, at 20 secs integration; Transmission ATR-FTIR (Perkin-Elmer *Spectrum 100*) over 4000-650 cm^{-1}, at 4 cm^{-1} resolution and 16 averaged scans. Tensile tests, without notch, were done on an *INSTRON 5566* with a 500 N load cell (*ASTM D1424-09*), on rectangular-shaped samples (60 x 25 x 4 mm; l x w x h), and 20 mm gauge length, at a constant extension rate of 100 mm.min^{-1}.[3]

2. Results

2.1 Alginate Precursor Chemical Characterisation

In positive MALDI-TOF MS spectra, molecules are commonly detected in proton adduct ([M+1] Da) or other adduct forms, e.g., sodium adduct ([M+23] Da). Figure S1 indicates various clusters with mass interval of 176 Da (i.e.; alginate uronic acid residues) were detected, which was consistent with past literature reports.[6–9] The monomer form seemingly predominates in the precursor.

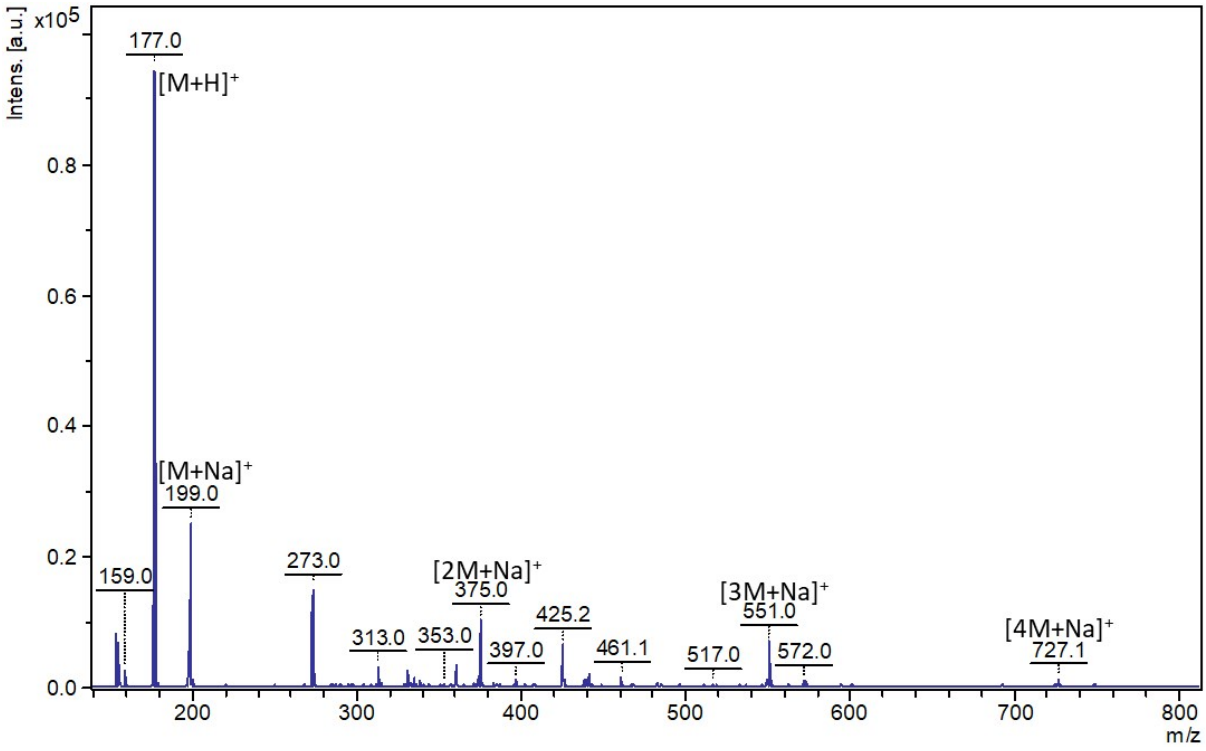

Figure S1. A positive MALDI-TOF MS spectrum for sodium alginate precursor. The assigned peaks correspond to; unsaturated monosacharrides (both proton adduct, $[M+H]^+$, and sodium adducts $[M+Na]^+$); unsaturated disaccharides (sodium adducts), unsaturated trisaccharides (sodium adducts), etc. Unassigned peaks are either noise or matrix peaks.

M:G estimates from the Raman $M_{\sim 975\ cm^{-1}}/G_{\sim 825\ cm^{-1}}$ and FTIR $M_{\sim 1030\ cm^{-1}}/G_{\sim 1080\ cm^{-1}}$ peak ratios indicate starting values of 1.76 ±0.27 and 0.66 ±0.78 respectively, in the alginate precursor (see Figure S2).

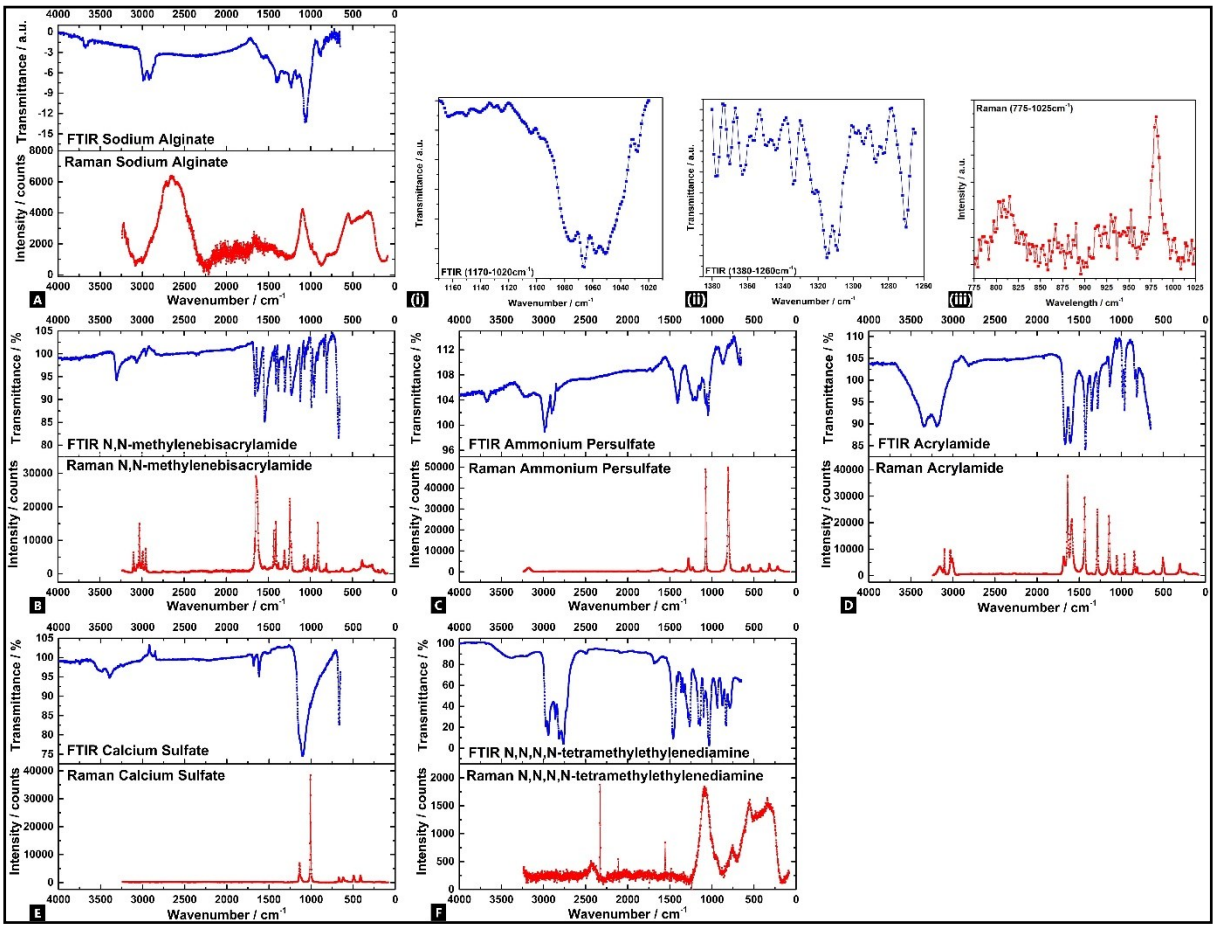

Figure S2. Fourier-transform infra-Red (FTIR) transmission spectra and Raman spectra for each individual precursor component involved in the formation of double network alginate-acrylamide tough hydrogel co-polymer systems

2.2 Time-Lapsed Imaging Data

Time-resolved confocal fluorescence microscopy image processed outputs, as labelled with a fluorescent R6G tracer dye, can be observed in Figure S3A. These direct visualisations of the detailed, dynamic, state-of-change structural movements and conformal organisations involved in tough hydrogel polymerisation processes show that clear changes that occur over the course of the reaction, most markedly within the first ~10 mins.[10–17] The corresponding digital microscopy images of the dynamic gel formation process are also readily observable (Figure S3B). The corollary photographic images (Figure S3C) of the reaction process, involving the R6G tracer dye, are also given. In all cases, the gelation process, onset of gelation and the attendant changes in the surface and broader structural properties can be clearly observed. The corresponding videos, in high spatial and temporal resolution, are available for all three data sets and included as attachments (*Figure V1-V3*).

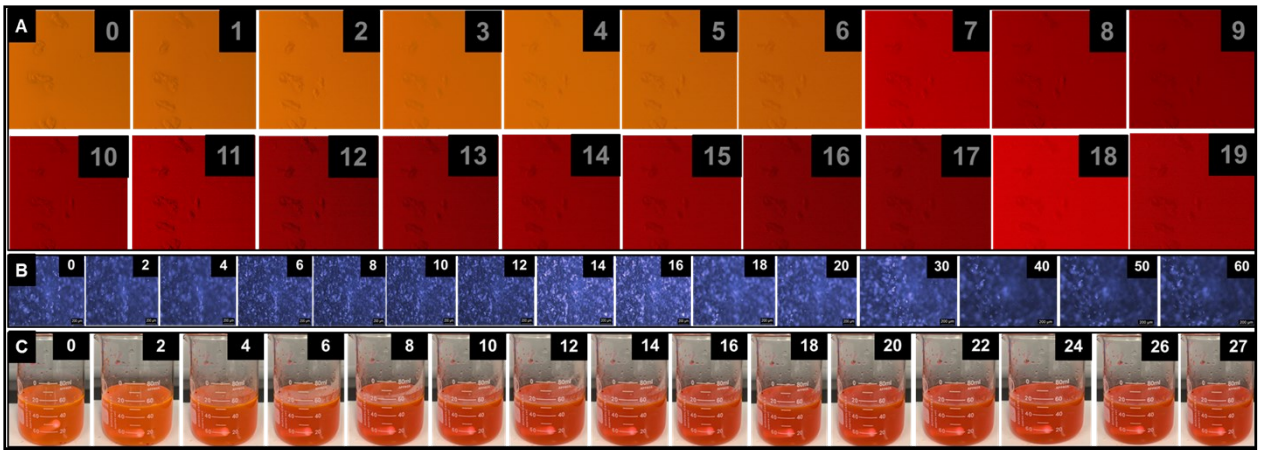

Figure *S3. Time-lapsed imaging of the alginate-acrylamide double-network tough hydrogel system via; fluorescence imaging in the presence of R6G tracer dye (A); digital microscopy (B) and real-time video monitoring (C). [NB: The approximate time lapsed (mins) is denoted in the top-right corner].*

2.3 Time-resolved Dynamic Light Scattering (DLS) and Zeta(ζ)-Potential Data for Tough Hydrogel Reaction Mixture

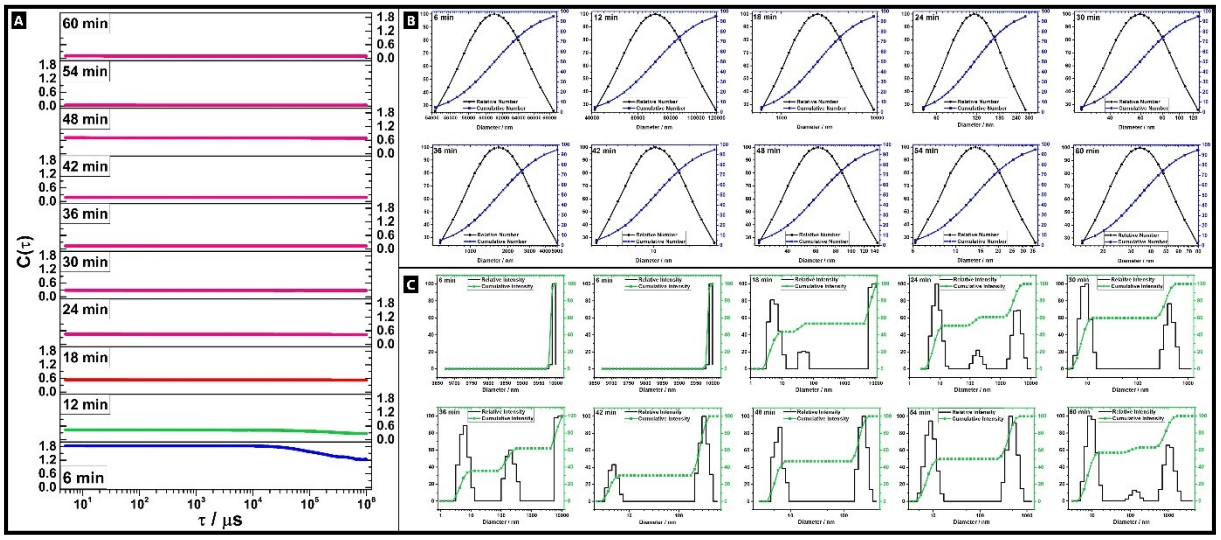

Figure S4. Time-resolved plots of double network alginate-acrylamide tough hydrogel copolymer mixtures as they proceed through the gel formation process; A) Autocorrelation function plots; B) Log-normal plots, and; C) Mean square deviation plots.

DLS allows the probing of particles across a sol–gel transition in non-ergodic samples like gels, from fluctuations in scattered light intensity on a microsecond timescale, due to the Brownian movement of the particles. These fluctuations were interpreted in terms of the autocorrelation function (ACF). Log-normal time lapse data in correllograms shows almost all datasets are skewed and have a long tail to the right of the mean; both the final and the intermediate relaxation become slower with time, which is a characteristic decay rate of out-of-equilibrium systems (Figure S4B).[18]

In the initial 6 minute phase, there is a large gradient, indicating a relatively fast decay, which corresponds to smaller particles. The decay represents an indirect measure of the time taken for particles to change their relative positions. As the size increases, decay increases to longer time periods. For the next (i.e.; 6-12 minute) phase, the gradient is muted and from the third section onwards, there were no discernible gradients observed; there is a plateau in the ensemble-averaged normalized field autocorrelation function.[19] The decay lines are not especially steep (the gradient is an indication of sample polydispersity), indicating greater sample polydispersity – unsurprising due to formation of the interpenetrating gel network over this reaction period. By the 3rd run (i.e.; beyond ~12 minutes), the rate of decay change is minimised; perhaps indicating onset of the gel point, which broadly correlated with the visible onset of gelation. This is also reflected in the lognormal and mean square deviation data whereby detected diameters decrease due to the gelation causing agglomeration of the copolymer structure (Figure S4C-D).

The gel point as obtained at the critical concentration (C*), corresponds to the onset of the entangled regime and signifies where the growing polymer chains interact with, and become physically entangled with eachother in solution; a loss in ergodicity.[20,21] This is in accordance with reptation theory whereby a decrease in the co-efficient of translational diffusion, due to increasing lack of free movement within constrained networks (unlike an unbound solution), increases both the viscosity and relaxation times.[20–22] Beyond C*, reaction dynamics are primarily and increasingly controlled by the entanglements (in turn dependent on both the ionic and covalent cross-links occurring in the system) within the polymeric nanogel structure, which confers enhanced network stability.[20,23] Thus, as the tough hydrogel network undergoes extensive entanglement, cross-linking and shear-thickening in the agglomerating system, with a shift in balance between the intramolecular and intermolecular associations, polymer segments are restricted by the cross-links to particular regions of the sample, such that only limited Brownian motions are possible, about a fixed average position (i.e.; the signal changes slowly and the correlation persists over a longer time period).[24] Increased shear flow results, which stretches macromolecular chains of increasing molecular weight leading to a higher probability of intermolecular associations, an increase in viscosity, and a consequent decrease in mobility.[25] This mechanically stabilised, extensively cross-linked structure is fundamentally controlled by the topological constraints enforced by the hydrogel network (i.e.; the array of obstacle points at which adjacent chain motions are prevented due to cross-linking and/or physical entanglement). This includes the dynamics of the macromolecules and extent of chain folding in response to variation in precursor molecular weights, on equilibrium properties (e.g.; onset of gelation, speed and extent of cross-linking, ratio of ionic/covalent crosslinks within the system etc).[22,26,27] This then, results in a reduction in the ACF, as clusters exhibit slow diffusion and internal fluctuations as well as longer correlations.[24,28]

2.4 Thermogravimetric Analysis (TGA) & Differential Scanning Calorimetry (DSC) Analysis

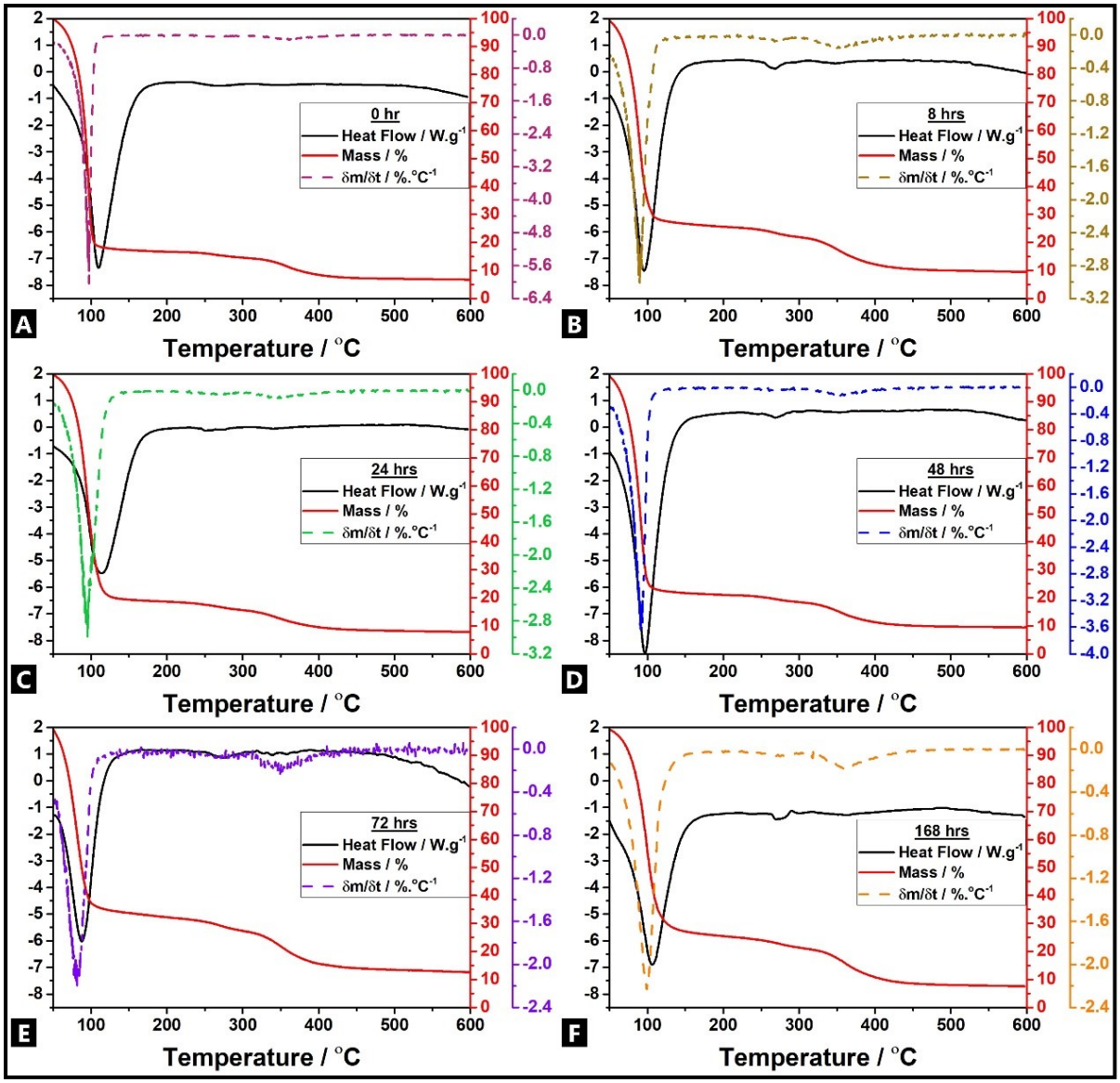

Figure S5. Time-resolved TGA and dTGA plots of double network alginate-acrylamide tough hydrogel co-polymer mixtures as they proceed through the gel formation process, and time-resolved DSC plots of double network alginate-acrylamide tough hydrogel co-polymer mixtures as they proceed through the gel formation process.

Evaluation of hydration and thermal decomposition of the alginate-PAAm tough hydrogel is described using thermogravimetric analysis (TGA) and differential scanning calorimetry (DSC) over the time-resolved cross-linking process (Figure S5). TGA thermograms in N_2 showed three discrete steps[29–33]:

1) Dehydration (~55-150ºC; ~80%): water loss from the hydrogel, either from the water contained within the main body of the gel, or from breakdown of the G- and M-units;
2) Decomposition (~230-300ºC; ~10%): formation of a carbonaceous residue due to the alginate polymer chain decomposition,[34,35] and;
3) Carbonate Formation (~325-450ºC; ~5%): Na_2CO_3 and/or $CaCO_3$ formation.

All variants show similar degradation patterns and the three stated transitions, indicating greater thermal stability arising from extending cross-linking processes.[36] As the hydrogel forms and cures, there is a change in both the first and second transition onset and maximum temperatures, as detected, with changes most apparent after 168 hrs. This indicates and supports the idea of structural rearrangements giving rise to enhanced bonding interactions and so improved strength in the tough hydrogel system, leading to increasing thermal stability. This includes the prolonged transition of the dehydration stage, as the water content is more effectively trapped within the gel network. Furthermore, denser packing in a local mixture affords a higher degradation temperature; e.g.; the degradative exothermic peak at the ~240°C region.[31,37] The relative %-weight loss across the cured systems also differs markedly; with increased aging, the amount of material formed during the carbonate formation stage increases, as a result of the more extensive ionic cross-linking yielding improved thermal resistance. Thus, it takes more energy to break the Ca^{2+} alginate cross-linked structure through dehydration of the saccharide rings and breaking of the C–O–C glycosidic bonds in the main chain of the polysaccharide, decomposition of the C-C bonds. The final products obtained are the thermally stable carbonates that retain some proportion of residues.[38]

Reverse-flow DSC thermograms were in broad agreement with the TG data. An initial endothermic peak at ~105°C, with the onset at ~67°C, thought due to moisture loss from the hydrogel. An endothermic peak at ~275°C with the onset at ~268°C is assigned to melting (T_m) of the polymer sample; the decomposition of the alginate superstructure due to partial decarboxylation of the protonated carboxylic groups and oxidation reactions of polyelectrolytes. A third expected endothermic peak is not observed, but would otherwise have been expected at ~350°C and attributed to full decomposition of the polymer. The lack of experimental transition is presumed due to the extensive decomposition and loss from the major two decomposition steps. All these endothermic transitions broadly tend to increase in line with aging, which indicates the increased crosslinked copolymerisation, structural rearrangement, denser packing and bulkiness of the alginate-acrylamide structure; the T_g broadened due to water more effectively trapped within the gel network, leading to increased thermal stability.[34–36,38]

2.5 Time-Resolved X-Ray Diffractograms of Forming Tough Hydrogels

Over the course of the reaction, there is no change in the long-range structural order; the standard non-crystalline diffractrograms representative of component polymeric structures and the broader superstructure that is formed (Figure S6). Thus, there are no apparent diffraction peaks observed and none that evolve over the course of the reaction. This includes no apparent areas of crystallisation within the restricted network of the gel matrix at any point, unlike past reports.[39,40]

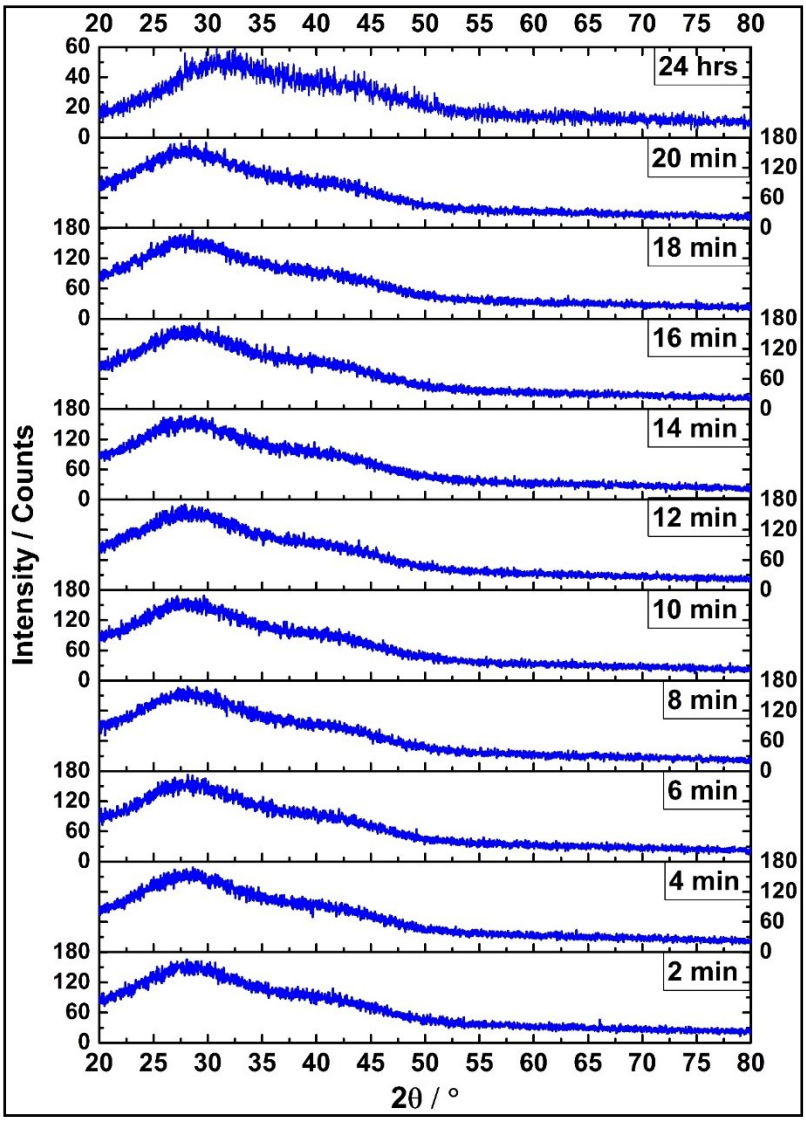

Figure S6. Time-resolved X-ray diffraction (XRD) patterns of double network alginate-acrylamide tough hydrogel co-polymer mixtures as they proceed through the gel formation process.

2.6 UV-vis Spectroscopy Precursor Reference Data

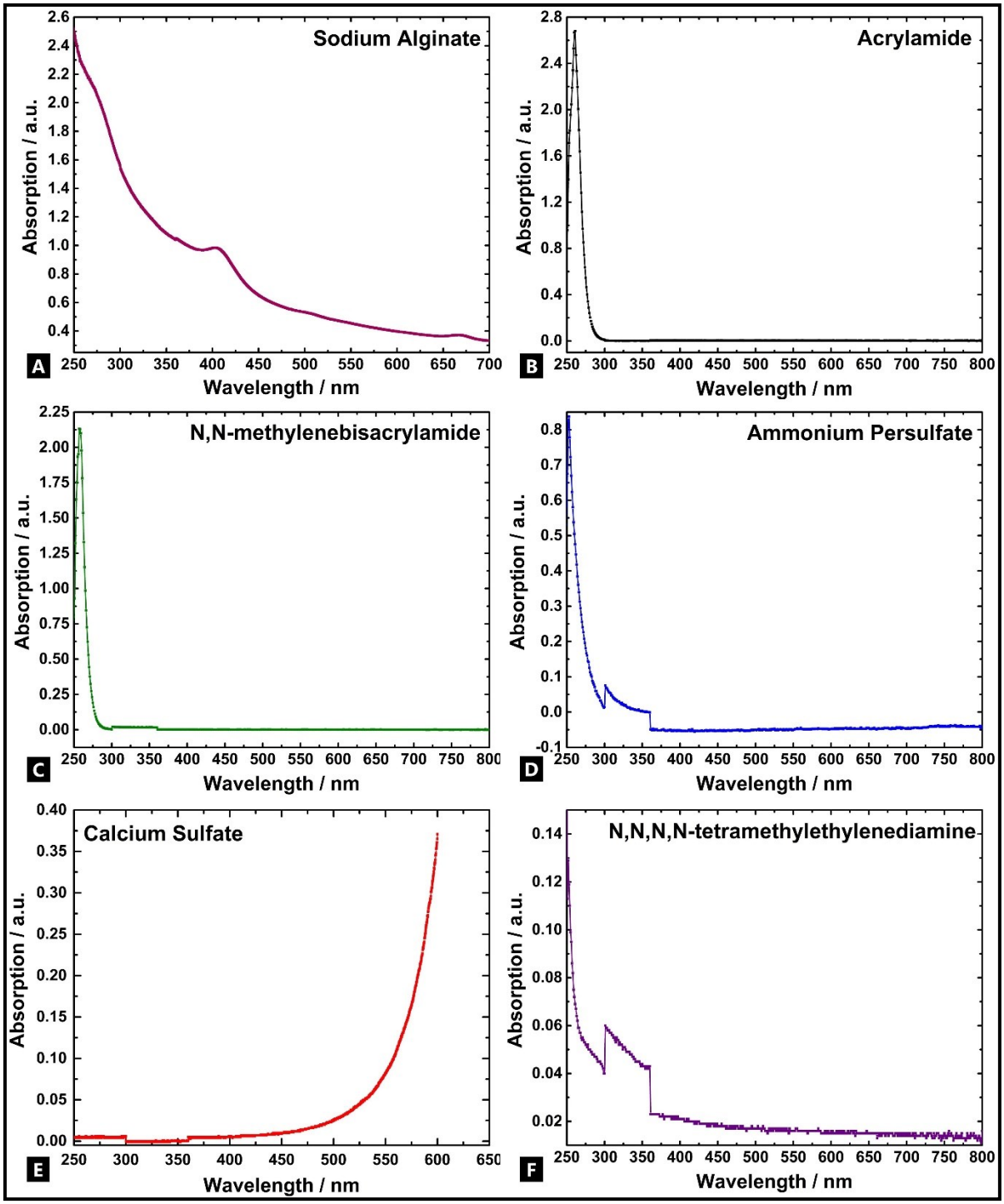

Figure S7. Ultraviolet-visible light (UV-vis) absorption spectra for each individual precursor component involved in the formation of double network alginate-acrylamide tough hydrogel copolymer systems.

2.7 Alternative Cationic Cross-linkers – Raman Analysis and Mechanical Testing

In order to test the variation of findings in response to changing the identity of $CaSO_4$ ionic cross-linker, four further cross-linkers were also studied in a time-resolved manner, using Raman spectroscopy and mechanical testing analysis. The four alternative, water-soluble, ionic cross-linkers were calcium chloride ($CaCl_2$), the amorphous calcium lignosulfonate (CaLs), sodium sulfate (Na_2SO_4) and magnesium sulfate ($MgSO_4$) – all at the equivalent mole ratio in the reaction mixture, as for the $CaSO_4$. Generally, different cations will effect different cross-linking responses and densities, as a result of both the cation oxidation state, as well as the relative solubility of the compound, e.g.; alginate-PAAm cross-linked by trivalent cations is reportedly stronger than for di-valently cross-linked.[41–43] All other aspects of the experiment were kept constant, so the linear charge density of the polyanion was even across the different systems.[44]

Of the samples, $CaCl_2$ showed uneven gelation and even exudation, while at the other extreme, CaLs showed extremely poor gelation, as signified by the inability to carry out any type of mechanical testing, even after two weeks of aging. This arrangement corresponds with the relative hydration free energies of the compounds.[45,46] This was reflected anecdotally in the relative stickiness of the gel samples, in the order $CaCl_2 > Na_2SO_4 > MgSO_4 > CaSO_4 >$ CaLs. This varying affinity with water is also thought to drive the interaction with uronic acid groups on the alginate structure.[45] For example, in the case of CaLs there is significant presence of hydrophilic sulfonate groups on the large anion.[47] However, the broader structure is hydrophobic, such that LS is frequently used as a dispersant. Thus, this dispersing behaviour results in a decrease in chain entanglements and intermolecular interactions on alginate, and low copolymerisation of AAm, resulting in a less viscous and structurally integral, hydrogel structure.[47–50]

Raman spectroscopic analysis was done over 0-60 mins and the 24-168 hr periods (Figure S8). As expected, all samples predominantly comprised alginate and acrylamide signals. In addition, the precursor source changes cross-linking time, e.g.; the poorer water solubility of $CaSO_4$ affords slow cross-linking by dissociated Ca^{2+}, yielding homogeneous hydrogels, whereas highly soluble $CaCl_2$ fosters fast cross-link, for inhomogeneous hydrogels.[41] Of the different ionic crosslinkers, each has a different property to the main $CaSO_4$ sample explored; CaLs has a large, complex polydisperse anion that is likely sterically hindered and should result in poor gelation properties. Na_2SO_4 has a lower charge, and $CaCl_2$ has a faster compound solubility; both should result in faster cross-linking kinetics. $MgSO_4$ is a larger cation, but with much the same reaction profile as $CaSO_4$.[51,52,61,53–60]

From the Raman spectroscopy data, the calculated M/G ratio indicates that the MgSO4 follows a similar route to $CaSO_4$, the Na_2SO_4 follows the reverse, while the CaLs seems to undergo very little M-block or G-block coordination initially (Figure S9). Broadly. the difference may partly be related to the variation between number and stability of cross-links formed; the Na_2SO_4 allowing for fast gelation with a great number of cross-links formed, but the Ca^{2+} affording the more stable bonding arrangements as a result of undergoing dimerization prior to further complexation.[45,62]

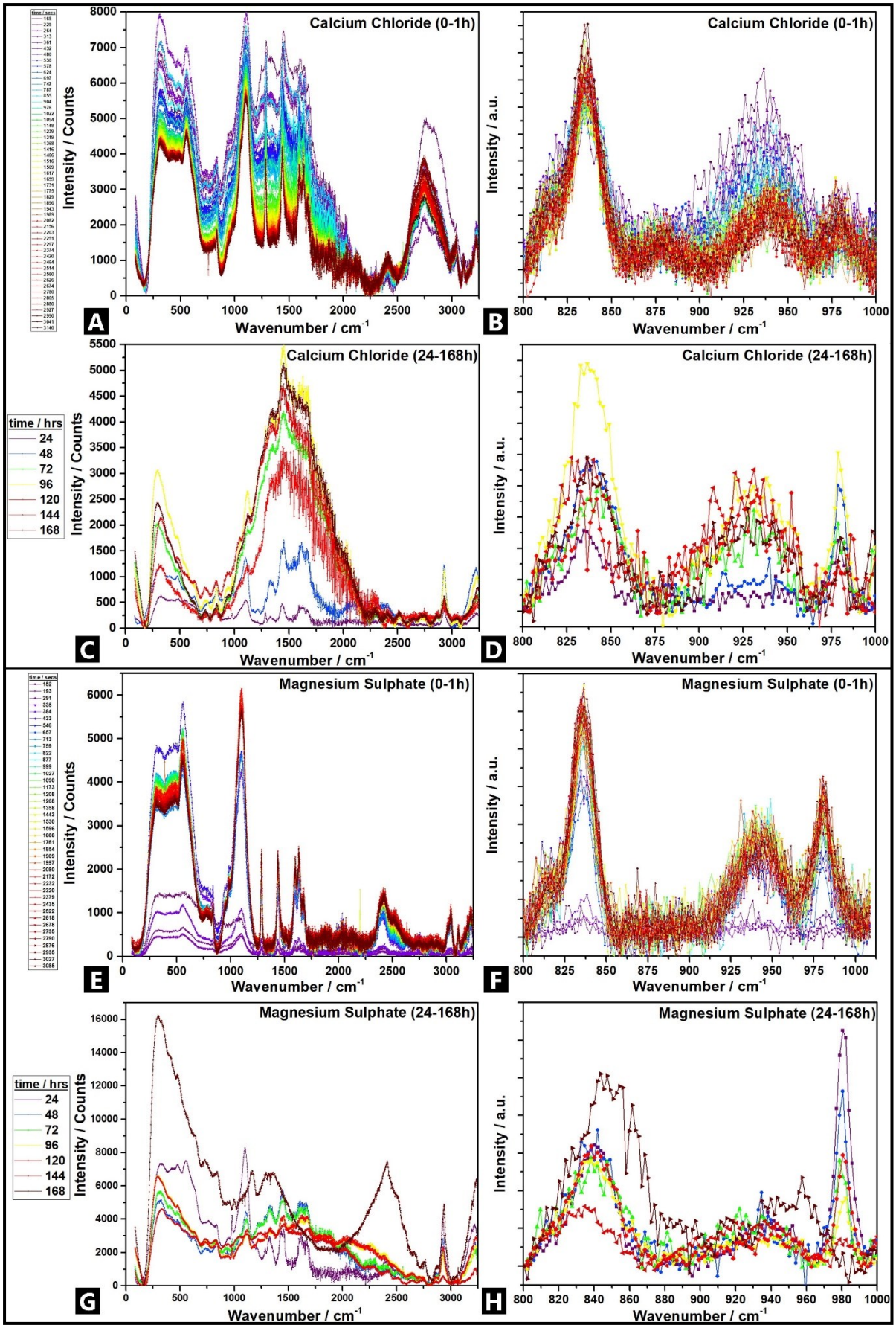
Calcium Chloride (0-1h)
Intensity / Counts
Wavenumber / cm-1
A
Intensity / a.u.
B
Calcium Chloride (24-168h)
C
D
time / hrs
24
48
72
96
120
144
168
Magnesium Sulphate (0-1h)
E
F
Magnesium Sulphate (24-168h)
G
H

1

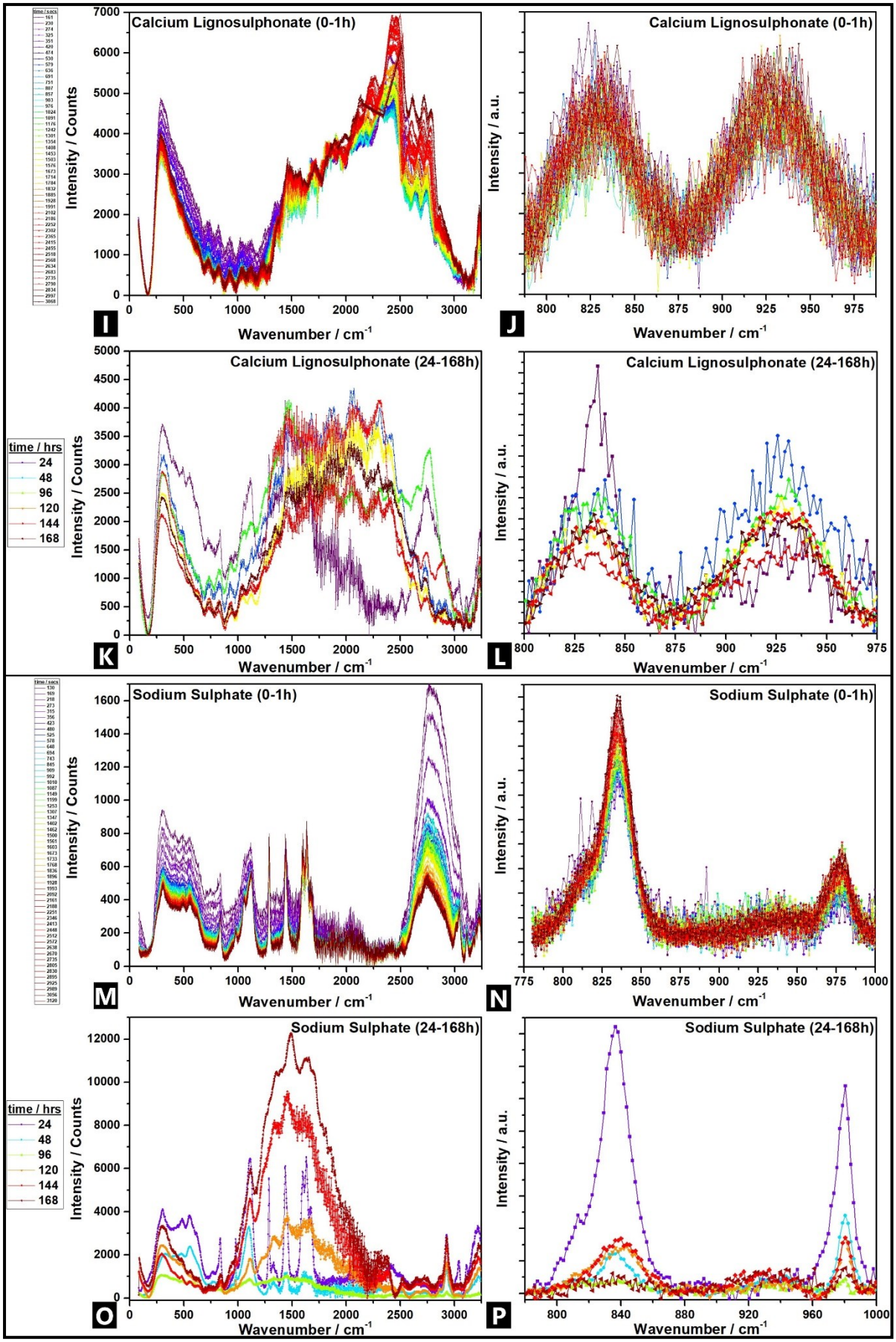
Calcium Lignosulphonate (0-1h)
Intensity / Counts
Wavenumber / cm-1
I
Calcium Lignosulphonate (0-1h)
Intensity / a.u.
Wavenumber / cm-1
J
Calcium Lignosulphonate (24-168h)
Intensity / Counts
Wavenumber / cm-1
K
Calcium Lignosulphonate (24-168h)
Intensity / a.u.
Wavenumber / cm-1
L
time / hrs
24
48
96
120
144
168
Sodium Sulphate (0-1h)
Intensity / Counts
Wavenumber / cm-1
M
Sodium Sulphate (0-1h)
Intensity / a.u.
Wavenumber / cm-1
N
Sodium Sulphate (24-168h)
Intensity / Counts
Wavenumber / cm-1
O
Sodium Sulphate (24-168h)
Intensity / a.u.
Wavenumber / cm-1
P

Figure S8. Raman spectra of a double network alginate-acrylamide tough hydrogel system over time, for CaCl2 (for 0-60 minute period (full spectrum (A); baselined M/G region of interest (B) and 24-168 minute period (full spectrum (C); baselined M/G region of interest (D)); $MgSO_4$ (for 0-60 minute period (full spectrum (E); baselined M/G region of interest (F) and 24-168 minute period (full spectrum (G); baselined M/G region of interest (H)); CaLs (for 0-60 minute period (full spectrum (I); baselined M/G region of interest (J) and 24-168 minute period (full spectrum (K); baselined M/G region of interest (L)), and; Na_2SO_4 (for 0-60 minute period (full spectrum (M); baselined M/G region of interest (N) and 24-168 minute period (full spectrum (O); baselined M/G region of interest (P)) .

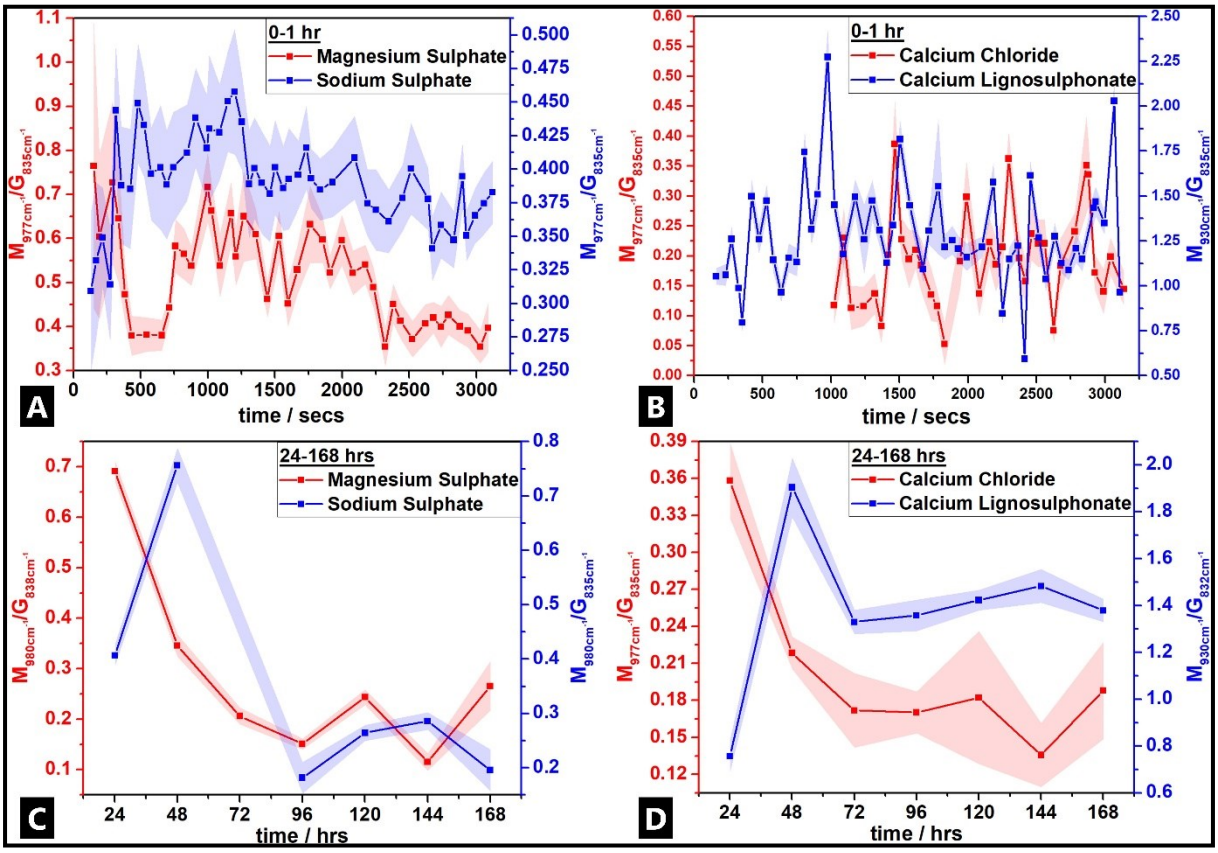

Figure S9. Alginate M/G ratio variations over time as calculated from Raman spectroscopy data, over the 60 minute (A-B) and 24-168 hr ranges (C-D) for $CaCl_2$, CaLs, $MgSO_4$, and Na_2SO_4 ionically cross-linked double network alginate-acrylamide tough hydrogel systems.

The double network tough hydrogels showed varying mechanical behaviour as a result of ionic cross-link precursor variation (see Figure S10). Incidentally, all recorded properties were inferior to the $CaSO_4$ precursor. It was not possible to obtain any testable samples at any time period for the CaLs-based cross-linked gels, indicating the poor network-forming and aggregating ability of the cross-linker. The highest tensile strength (~232 kPa), Young's modulus (~195 kPa), and toughness (~599 kJ/m^3) values were recorded for the $CaCl_2$ variant, while maximal strain (~123%) was afforded by the $MgSO_4$ ionic cross-linked system. Thus, variation of ionic cross linker has a clear impact on the mechanical properties, which is intrinsically tied to the extent of physical cross-linking that occurs.

Over the course of 168 hrs, the maximum strain ($strain_{max}$) for all samples falls from 4 hrs to the 48 hr mark, before increasing to 168 hrs. The higher $strain_{max}$ at 4 hrs is possibly due to the hydrogel still undergoing reversible, complex breaking and reformation cross-linking processes with chain undulation. This then results in readily extensible polymer chains. The absence of structural robustness at 4 hrs is also why the tensile strength values are at their lowest point. The resultant high strain after

168 hrs indicate the structural strength induced in the hydrogel body over ageing time due to strain hardening. From ~24-48 hrs onwards, the structure of the different double hydrogels seem to become more stable and chain-unfolding does not occur as easily as at 4 hrs. As the reaction proceeds with ageing and the hydrogel dehydrates, the $strain_{max,}$ tensile strength, modulus, and toughness further increase.

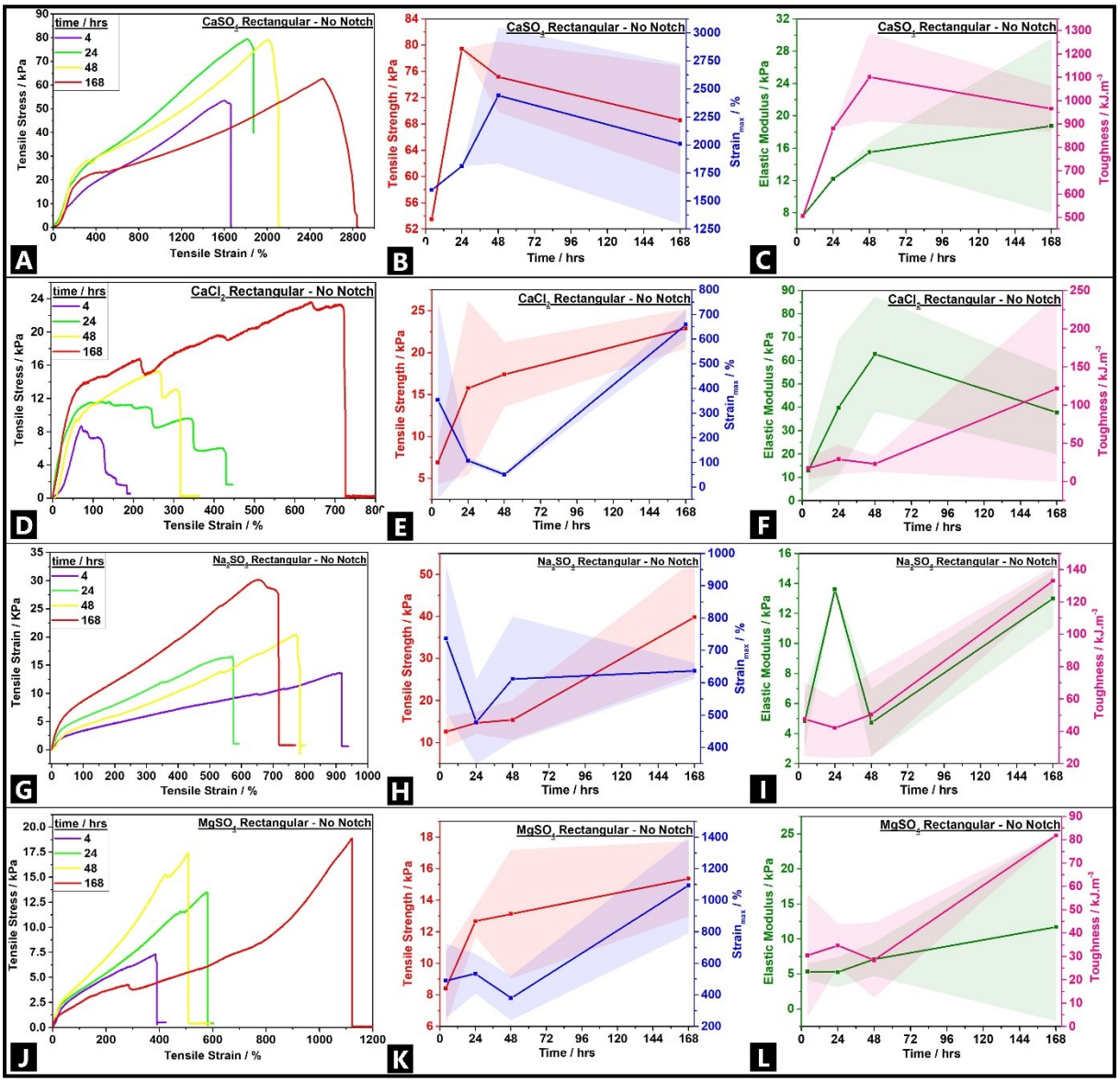

Figure S10. Time dependent variation in tensile strain–stress curves of rectangular notch-less specimens, and calculated tensile strength, stain %, elastic modulus and toughness for $CaSO_4$ (A-C); $CaCl_2$ (D-F); CaLs (G-I), and; $MgSO_4$ (J-L)) cationically cross-linked alginate-acrylamide tough hydrogel systems.

2. References

1 M. Cavo, M. Caria, I. Pulsoni, F. Beltrame, M. Fato and S. Scaglione, *Sci. Rep.*, 2018, **8**, 5333.

2 A. D. Strong and R. L. Daniels, *BMC Cancer*, 2017, **17**, 516.

3 Y. Xiao, E. A. Friis, S. H. Gehrke and M. S. Detamore, *Tissue Eng. Part B Rev.*, 2013, **19**, 403–412.

4 E. Meijering, I. Smal, O. Dzyubachyk and J.-C. Olivo-Marin, in *Microscope Image Processing*, eds. Q. Wu, F. A. Merchant and K. R. Castleman, Elsevier Academic Press, 2008, pp. 401–440.

5 S. Delpretti, F. Luisier, S. Ramani, T. Blu and M. Unser, in *2008 5th IEEE International Symposium on Biomedical Imaging: From Nano to Macro*, IEEE, 2008, pp. 149–152.

6 D. Kulig, A. Zimoch-Korzycka, A. Jarmoluk and K. Marycz, *Polymers (Basel).*, 2016, **8**, 167.

7 N. Flórez-Fernández, H. Domínguez and M. D. Torres, *Int. J. Biol. Macromol.*, 2019, **124**, 451–459.

8 T. M. Aida, T. Yamagata, M. Watanabe and R. L. Smith, *Carbohydr. Polym.*, 2010, **80**, 296–302.

9 G. Gonzalez-Gil, L. Thomas, A.-H. Emwas, P. N. L. Lens and P. E. Saikaly, *Sci. Rep.*, 2015, **5**, 14316.

10 M. Abadi, M. F. Serag and S. Habuchi, *Nat. Commun.*, 2018, **9**, 5098.

11 I. Semenova and V. Rodionov, in *Microtubule Protocols*, Humana Press, 2007, pp. 93–102.

12 Liang Yuan, Y. F. Zheng, J. Zhu, Lina Wang and A. Brown, *IEEE Trans. Med. Imaging*, 2012, **31**, 117–130.

13 S. Onogi, H. Shigemitsu, T. Yoshii, T. Tanida, M. Ikeda, R. Kubota and I. Hamachi, *Nat. Chem.*, 2016, **8**, 743–752.

14 J. R. Kuhn and T. D. Pollard, *Biophys. J.*, 2005, **88**, 1387–1402.

15 D. Muzzey and A. van Oudenaarden, *Annu. Rev. Cell Dev. Biol.*, 2009, **25**, 301–327.

16 O. Dzyubachyk, W. A. van Cappellen, J. Essers, W. J. Niessen and E. Meijering, *IEEE Trans. Med. Imaging*, 2010, **29**, 852–867.

17 F. Zou and L. Bai, *Methods*, 2019, **159–160**, 138–145.

18 V. Kapishon, R. A. Whitney, P. Champagne, M. F. Cunningham and R. J. Neufeld, *Biomacromolecules*, 2015, **16**, 2040–2048.

19 S. Rose, A. Marcellan, D. Hourdet, C. Creton and T. Narita, *Macromolecules*, 2013, **46**, 4567–4574.

20 E. A. S. Doherty, C. W. Kan and A. E. Barron, *Electrophoresis*, 2003, **24**, 4170–4180.

21 W. A. de Morais, M. R. Pereira and J. L. C. Fonseca, *Carbohydr. Polym.*, 2012, **87**, 2376–2380.

22 T. C. B. McLeish, *Adv. Phys.*, 2002, **51**, 1379–1527.

23 P. Kujawa, A. Audibert-Hayet, J. Selb and F. Candau, *Macromolecules*, 2006, **39**,

384–392.

24 J. G. H. Joosten, J. L. McCarthy and P. N. Pusey, *Macromolecules*, 1991, **24**, 6690–6699.

25 E. J. Regalado, J. Selb and F. Candau, *Macromolecules*, 1999, **32**, 8580–8588.

26 D. Wentzel and W. Oppermann, *Colloid Polym. Sci.*, 1997, **275**, 205–213.

27 J. D. Hoffman and R. L. Miller, *Polymer (Guildf).*, 1997, **38**, 3151–3212.

28 C. Rochas and E. Geissler, *Macromolecules*, 2014, **47**, 8012–8017.

29 I. Khalid, M. Ahmad, M. Usman Minhas, K. Barkat and M. Sohail, *Adv. Polym. Technol.*, 2018, **37**, 985–995.

30 H. Zhu, Q. Zhang and S. Zhu, *ACS Appl. Mater. Interfaces*, 2016, **8**, 17395–17401.

31 G. C. Fontes, V. M. A. Calado, A. M. Rossi and M. H. M. Da Rocha-Leão, *Biomed Res. Int.*, 2013, **2013**, 1–11.

32 S. Jana, M. Kumar Trivedi and R. M. Tallapragada, *Pharm. Anal. Acta*, , DOI:10.4172/2153-2435.1000430.

33 J. P. Soares, J. E. Santos, G. O. Chierice and E. T. G. Cavalheiro, *Eclet. Quim.*

34 A. Akın and N. Işıklan, *Int. J. Biol. Macromol.*, 2016, **82**, 530–540.

35 G. Nandi, A. Changder and L. K. Ghosh, *Carbohydr. Polym.*, 2019, **215**, 213–225.

36 P. Pal, J. P. Pandey and G. Sen, *Int. J. Biol. Macromol.*, 2018, **113**, 1116–1124.

37 D. C. Furuya, S. A. da Costa, R. C. de Oliveira, H. G. Ferraz, A. Pessoa Junior and S. M. da Costa, *Mater. Res.*, 2017, **20**, 377–386.

38 M. M. Ghobashy and G. Bassioni, *Adv. Polym. Technol.*, 2018, **37**, 2123–2133.

39 H. S. Samanta and S. K. Ray, *Carbohydr. Polym.*, 2014, **106**, 109–120.

40 H. S. Samanta and S. K. Ray, *Carbohydr. Polym.*, 2014, **99**, 666–678.

41 M. Anurup, R. Monika, M. Rabibrata, B. Provas and C. Jyotirmoy, *Front. Bioeng. Biotechnol.*, , DOI:10.3389/conf.FBIOE.2016.01.00171.

42 H. Jiang, L. Fan, S. Yan, F. Li, H. Li and J. Tang, *Nanoscale*, 2019, **11**, 2231–2237.

43 R. V. Kulkarni and B. Sa, *J. Drug Target.*, 2008, **16**, 167–177.

44 H. D. Graham, *J. Food Sci.*, 1993, **58**, 539–543.

45 U. T. D. Huynh, A. Lerbret, F. Neiers, O. Chambin and A. Assifaoui, *J. Phys. Chem. B*, 2016, **120**, 1021–1032.

46 M. Yadav and K. Y. Rhee, *Carbohydr. Polym.*, 2012, **90**, 165–173.

47 R. P. Dumitriu, I. Stoica, D. S. Vasilescu, G. Cazacu and C. Vasile, *J. Polym. Environ.*, 2018, **26**, 1100–1112.

48 S. Gao, Z. Cheng, X. Zhou, Y. Liu, R. Chen, J. Wang, C. Wang, F. Chu, F. Xu and D. Zhang, *Int. J. Biol. Macromol.*, 2020, **161**, 755–762.

49 H. Zhou, D. Yang, X. Wu, Y. Deng and X. Qiu, *Holzforschung*, 2012, **66**, 825–832.

50 M. Abdollahi, M. Pourmahdi and A. R. Nasiri, *J. Pet. Sci. Eng.*, 2018, **171**, 484–494.

51 T. Baysal, N. Noor and A. Demir, *Polym. Technol. Mater.*, 2020, 1–30.

52 M. Liska, A. Wilson and J. Bensted, in *Lea's Chemistry of Cement and Concrete*, Elsevier, 2019, pp. 585–640.

53 R. Flatt and I. Schober, in *Understanding the Rheology of Concrete*, Elsevier, 2012, pp. 144–208.

54 S. Damiati, *Macromol. Res.*, , DOI:10.1007/s13233-020-8142-9.

55 N. Yu, Y. Xu, Q. Jiang and W. Xia, *Int. J. Food Prop.*, 2016, 1–14.

56 X. Le, W. Lu, J. Zheng, D. Tong, N. Zhao, C. Ma, H. Xiao, J. Zhang, Y. Huang and T. Chen, *Chem. Sci.*, 2016, **7**, 6715–6720.

57 L. Liu, X. Li, M. Nagao, A. Elias, R. Narain and H.-J. Chung, *Polymers (Basel).*, 2017, **9**, 558.

58 L. Fernandez, C. Alonso, A. Hidalgo and C. Andrade, *Adv. Cem. Res.*, 2005, **17**, 9–21.

59 S. T. Lee, H. Y. Moon, R. D. Hooton and J. P. Kim, *Cem. Concr. Res.*, 2005, **35**, 1314–1323.

60 D. R. M. Brew and F. P. Glasser, *Cem. Concr. Res.*, 2005, **35**, 85–98.

61 Y. L. Khromova, *Colloid J.*, 2006, **68**, 115–119.

62 I. Braccini and S. Pérez, *Biomacromolecules*, 2001, **2**, 1089–1096.